








Tetracarbonates in silicate melts may be at the origin of a deep carbon reservoir in the deep Earth

Valerio Cerantola ^{1,2,3✉}, Christoph J. Sahle ³, Sylvain Petitgirard ^{4,5}, Min Wu ⁶, Stefano Checchia ³, Christopher Weis⁷, Marco Di Michiel³, Gavin B. M. Vaughan³, Ines E. Collings³, Róbert Arató ^{5,8}, Max Wilke⁹, Adrian P. Jones¹⁰, Michael Hanfland³ & John S. Tse ¹¹

Much of Earth's carbon may have been stripped away from the silicate mantle by dense metallic-iron during core formation. However, at deep magma ocean conditions carbon becomes less siderophile and thus large amounts of it may be stranded instead in the deep mantle. Here, we describe the structure and compaction mechanisms of carbonate glass to deep mantle pressures. Our results, based on non-resonant inelastic X-ray scattering, X-ray diffraction and ab initio calculations, demonstrate a pressure-induced change in hybridization of carbon from sp^2 to sp^3 starting at 40 GPa, due to the conversion of $[^3]CO_3^{2-}$ groups into $[^4]CO_4^{4-}$ units, which is completed at ~112 GPa. The pressure-induced change of carbon coordination number from three to four increases possibilities for carbon-oxygen interactions with lower mantle silicate melts. sp^3 hybridized carbon provides a mechanism for changing the presumed siderophile nature of deep carbon, becoming a possible source for carbon-rich emissions registered at the surface in intra-plate and near-ridge hot spots.

¹ Department of Earth and Environmental Sciences, Università degli Studi di Milano-Bicocca, Piazza della Scienza 4, 20126 Milan, Italy. ² European XFEL, 4 Holzknapp, 22869 Schenefeld, Germany. ³ ESRF – The European Synchrotron, 71 Avenue des Martyrs, 38000 Grenoble, France. ⁴ Department of Earth Sciences, Institute of Geochemistry and Petrology, ETH, 8092 Zurich, Switzerland. ⁵ Bayerisches Geoinstitut, Universität Bayreuth, Bayreuth D-95440, Germany. ⁶ College of Materials Science & Engineering, Zhejiang University of Technology, Hangzhou 310014 Zhejiang, China. ⁷ Fakultät Physik/DELTA, Technische Universität Dortmund, 44227 Dortmund, Germany. ⁸ Isotope Climatology and Environmental Research Centre, Institute for Nuclear Research, H-4001 Debrecen, Hungary. ⁹ Institut für Geowissenschaften, Universität Potsdam, Karl-Liebknecht-Straße 24, 14476 Potsdam, Germany. ¹⁰ Earth Sciences, University College London Gower Street, London WC1E 6BT, UK. ¹¹ Department of Physics and Engineering Physics, University of Saskatchewan, Saskatoon, SK, Canada. ✉email: valerio.cerantola@unimib.it

The nature and properties of carbonate melts at high pressures (p) and temperatures (T) may govern the exchange of carbon between the Earth's interior and the atmosphere. Because of their low densities and viscosities at shallow depths (<5 GPa), carbonate melts can mobilize carbon out of subducting slabs and can segregate rapidly from the source regions, making them active factors in crustal and sub-crustal processes^{1,2}. The remarkable physical properties of carbonate melts, such as low viscosity³ and high electrical conductivity⁴, are best explained by the electronic structure of the CO_3^{2-} groups that lack unpaired orbitals for covalent bonding, and thus are unable to polymerize⁵, unlike the SiO_4^{4-} tetrahedron in silicate melts.

Experimentally, the behavior of carbonate melts at greater depths remains unexplored, despite the changes in physical and chemical properties that could be induced from compression-driven structural transformations, as observed e.g. in silicate glasses and melts^{6–8}. Indeed, melts' properties directly reflect on the chemical partitioning in the Earth, especially during core-formation where partial, or complete, mantle melting occurred through the formation of deep magma oceans (MO) which enabled the segregation of the metallic core⁹. During this process, the growing metallic core stripped away elements from the silicate mantle depending on their affinity, or siderophile character, carbon among them. Two recent studies^{10,11} reported a substantial change in the carbon partition coefficient between silicates and metals ($D_{C_{\text{metal/silicate}}}$) at $p > 40$ GPa, suggesting that carbon becomes more lithophile at depth and concentrated in the deep mantle, e.g. bonding into the structure of silicate melts. Recent simulations show a progressive increase in polymerization in C-bearing silicate melts at rising pressures, which is evidenced by a decrease in CO_2 and CO_3 species at the expense of CO_4 and more complex oxo-carbon polymers (C_xO_y)^{12–14}. The same studies also report that at highly reducing conditions the presence of Fe-C, Si-C, C-C, and C-H clusters in the melts hints toward carbon partitioning from the liquid silicate to the metallic core. However, the extent to which carbon becomes less siderophile at extreme pressures and temperatures is still unknown and the underlying physical phenomena remain elusive.

Here we report the pressure-induced changes in the atomic and electronic structure of the carbonatitic glass $\text{K}_2\text{Mg}(\text{CO}_3)_2$ (Methods), used as an analog for carbonate melts^{5,7,8} up to pressures near the core mantle boundary (CMB). Our results provide experimental evidences for the hybridization change in C atoms from sp^2 to sp^3 at $p > 40$ GPa, which directly relates to the change in D_C in the Earth's lower mantle. We used a combination of synchrotron-based techniques, non-resonant inelastic X-ray scattering (XRS) at the oxygen K-edge and X-ray diffraction via pair distribution function (PDF) analysis, to monitor the evolution of the electronic structure and bond lengths upon compression of the glass (Methods). The interpretation of the experimental data is supported by ab initio Molecular Dynamic (AIMD) simulations and spectrum calculations based on solving the Bethe-Salpeter equation (Methods). $\text{K}_2\text{Mg}(\text{CO}_3)_2$ -glass was chosen for two reasons, (i) the high Mg content in the glass reflect the high abundance of Mg in the Earth's interior, hence making it suitable for experiments looking at simplified natural systems, and (ii) it is the simplest carbonate-glass stoichiometry quenchable at ambient conditions.

Results

X-ray Raman Scattering at the O K-edge. Figure 1 shows the oxygen K-edge XRS spectra for $\text{K}_2\text{Mg}(\text{CO}_3)_2$ at pressures ranging from 1 atm (Fig. 1a bottom) to 100 GPa (Fig. 1a top). The peak near 534 eV, more pronounced at lower pressures, reflects the anti-bonding molecular orbital of the resonant C=O double bond associated with the CO_3 planar unit, also known as π^* -resonance¹⁵.

At higher energies, above 538 eV, a second broader feature indicated as σ^* corresponds to the unoccupied C-O σ^* antibonding orbitals. The most prominent spectral change in the oxygen K-edge with pressure is the disappearance of the π^* -resonance at 534 eV (Fig. 1a, b), unambiguous evidence of the breakage of the C=O double bond. The integrated intensity of the π^* -feature as a function of pressure in Fig. 1c shows that this process occurs gradually. After an initial decrease between ambient conditions and 10 GPa, we observe a plateau in π^* -spectral intensity and a subsequent almost linear decay starting at ~ 40 GPa until the highest pressure, where extrapolation suggests a complete disappearance at ca. 112 GPa. Besides these prominent changes in the spectral shape, we observe a shift of spectral weight visible by a smooth intensity increase in the σ^* -resonance at pressures above 80 GPa, evidenced as the emergence of a peak at ~ 536 eV in the spectral-difference plot (Fig. 1b). We associate the spectral shift to higher energies to general compaction around the O atoms. Simulated XRS spectra based on atomic structural snapshots from AIMD simulations are shown as thin black lines in Fig. 1a, supporting our assessment of the formation of sp^3 hybridized $^{[4]}\text{CO}_4$ units at the expense of $^{[3]}\text{CO}_3$ (Fig. 2 and Supplementary Figs. 1 and 2).

Pair distribution function analyses. The PDFs in Fig. 3a show individual peaks representing well-defined cation-anion coordination shells, the first three being C-O, Mg-O, and K-O (Supplementary Fig. 3). Cation-cation and anion-anion peaks are located at larger distances (Supplementary Fig. 3). While Mg-O and K-O merge together upon compression, the first peak of the PDF (C-O) is well resolved up to the highest measured p -point. A detailed view of the PDFs in the vicinity of the C-O bond, is shown in Fig. 3b. After the initial compaction of the C-O distance between ambient pressure and 33 GPa, the initial C-O length is recovered at 46 GPa and increases up to 85 GPa, where it decreases again until the highest studied pressure of 104 GPa (Fig. 3 and Table 1). Above 85 GPa the C-O peak is also affected by a remarkable broadening at the FWHM, which shows that C-O distances at 104 GPa vary between 0.98 Å to 1.42 Å, (Table 1). Compared to crystalline tetracarboxates¹⁶, the C-O average bond length at 85 GPa of 1.323 Å is similar to those reported for i.e. $\text{Fe}_4\text{C}_3\text{O}_{12}$ at 74 GPa (1.352 Å) and $\text{Fe}_4\text{C}_4\text{O}_{13}$ at 97 GPa (1.337 Å). The expansion of the bonds to an average length similar to the C-O distance in CO_4 -units in crystalline tetracarboxate clearly indicates that at ~ 85 GPa more than 50% of the CO_3 -groups have been converted to CO_4 -groups, confirming the conclusions drawn from the XRS results and AIMD simulations (Supplementary Fig. 1). In the same pressure interval, the Mg-O bond expands to 1.98 Å (Supplementary Fig. 4 and Table 1), which suggests an increase of coordination environment to 7+ at 104 GPa, from the initial ~ 4.5 at 1 bar¹⁷. K-O bonds show an almost linear compression, with a kink on the compression rate at 46 GPa, which coincides with the onset of formation of $^{[4]}\text{CO}_4$ -groups. C-O, Mg-O, and K-O distances extracted from the AIMD simulations confirm these compression trends (Supplementary Figs. 4 and 5 and Supplementary Note 1).

Overall, the behavior of the carbonate glass at high pressures can be rationalized as follows (Supplementary Note 1):

0 – 40/45 GPa: filling of voids (mainly in the first 10 GPa), compaction with local atomic rearrangement and distortions.

40/45 – 85 GPa: breaking of C=O double bonds in $^{[3]}\text{CO}_3$ -groups and formation of $^{[4]}\text{CO}_4$ tetrahedra. Onset of polymerization in the glass.

>85 GPa: a fully polymerized framework structure with some local remnants of CO_3 -groups, up to ca. 112 GPa. Further compaction.

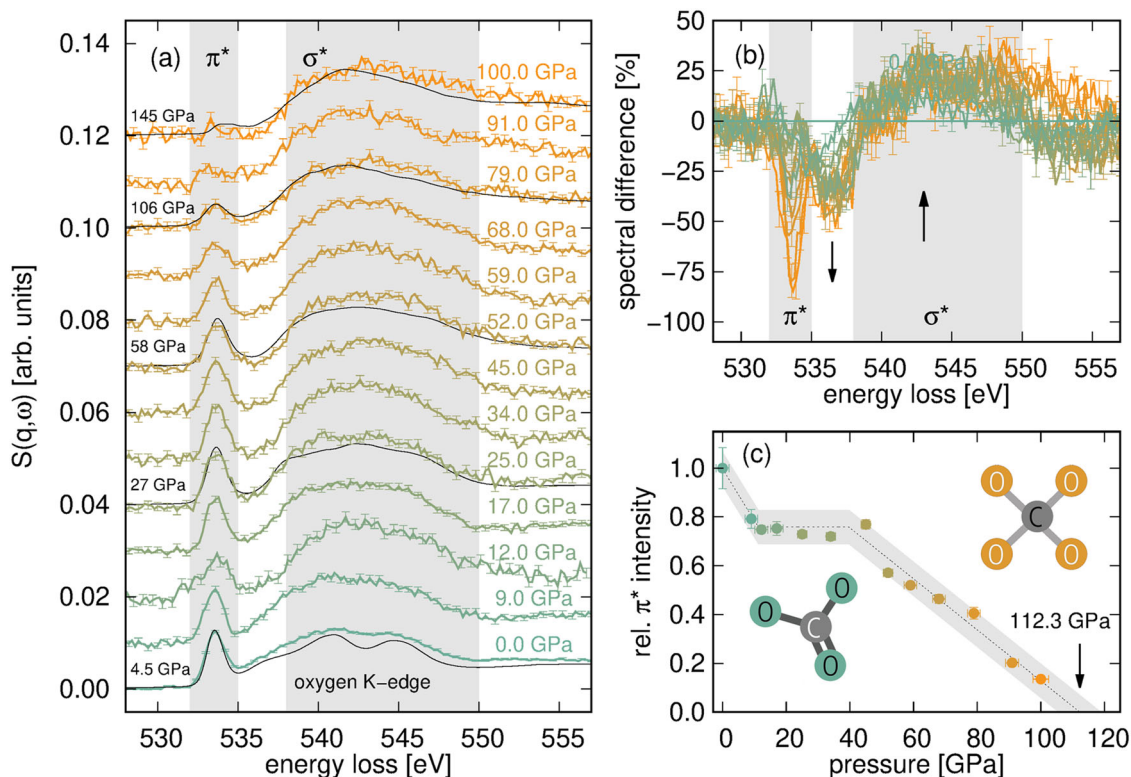


Fig. 1 Experimental and simulated data from XRS spectroscopy. **a** Oxygen K-edge XRS spectra of $K_2Mg(CO_3)_2$ glass at pressures between 1 bar and ~100 GPa. Simulated spectra are shown as thin black lines, the values on the left show the pressure at which the simulations were run. The simulated spectra are matched to the most similar experimental spectrum. Error bars present standard errors of the mean, i.e. standard deviation divided by the square root of the sample size. **b** Spectral differences with respect to the ambient data. The regions of the π^* - and σ^* -features are marked with shaded gray areas. **c** Integrated intensity of the π^* peak versus pressure. Intensity and pressure error bars represent the standard error given by the peak fitting procedure.

Our simulations show a modest increase in π^* -peak intensity when the glass is decompressed. However, as expected, the reversibility is far from complete because of the active kinetic barrier that hinders the reverse transformation, from 4-fold to 3-fold coordinated carbon (Supplementary Fig. 7).

Discussion

Carbon distribution in the deep Earth depends on the physico-chemical properties of carbon-complexes in melts along with their buoyancy. While most of the primordial carbon has been stripped away from the primordial mantle during core formation, recent estimates predict carbon concentration between 0.09(4) and 0.20(10) wt% C in the core¹¹, much lower than the 1 wt% previously assessed from cosmochemical and geochemical considerations¹⁸. Thus even with the lowest estimates, the core would still account for more than half of Earth's total carbon budget^{11,19}, the rest would reside in the mantle.

The effect of pressure and temperature on the oxygen fugacity (fO_2) of the Earth's lower mantle points toward a reducing environment, i.e. $fO_2 \sim IW-2$ log units^{20,21}, where carbon would preferentially bond with itself (C-C), hydrogen (C-H), iron (C-Fe), and silicon atoms (C-Si), when incorporated in silicate melts¹²⁻¹⁴. Irrespective of the origin of lower mantle carbon content, i.e. (i) carbon of primordial origin and (ii) contributions of subducted material of oceanic crust composition, the oxidation state in the deep mantle is probably inhomogeneous, consisting of locally or regionally oxidized domains. Several processes might influence the oxidation state of these regions, most important of all the disproportionation of metallic iron, which has caused the primordial lower mantle to have an excess of Fe^{3+} content (high

$Fe^{3+}/(Fe^{2+}+Fe^{3+})$ after metallic iron segregation down into the core²²⁻²⁴. This mechanism was also proposed to explain the Great Oxygenation Event (GOE), which happened between 2.0–2.5 Ga ago^{25,26} initiated with the onset of vertical mixing with subsequent subduction of slabs and a more global convection. It was also suggested by several studies an overall increase of the fO_2 in the MO during Earth's accretion, the natural consequence of a (i) late delivery of oxidized material from the outer disk (in form of carbonaceous phases and chondritic materials)^{27,28}, and (ii) the tendency of the redox reaction $SiO_2 + 2Fe \rightarrow 2FeO + Si$ to shift to the right as pressure and temperature increases (11 and refs in therein). We believe that at these conditions the presence of tetracarbonate is plausible, if not as single phases that would require fO_2 values too high to be found in a MO, i.e. at least 1 log units above the IW buffer at 45 GPa²⁹, but incorporated in silicate melts forming a number of different ionic complexes¹²⁻¹⁴. In fact, despite the large compositional difference between our simplified system and those reported in previous simulations¹², the pressure evolution of three- to four coordinated carbon species is consistent to those reported for C-bearing $MgSiO_3$ melts at lower mantle conditions. Even at reducing conditions where ~80% of carbon atoms are coordinated with each other forming carbon clusters, ~50% of carbon atoms are also bonded with at least one oxygen atom¹². Even if these results do not automatically imply the presence of tetracarbonate groups in the melt, they clearly demonstrate that carbon-oxygen interactions are not suppressed. Moreover, carbonated-silicate melts are also predicted as a result of redox melting processes in the reduced mantle at the CMB³⁰, and the formation of calcium carbonate was shown at the expenses of dolomite in the presence of iron metal in DAC experiments³¹.

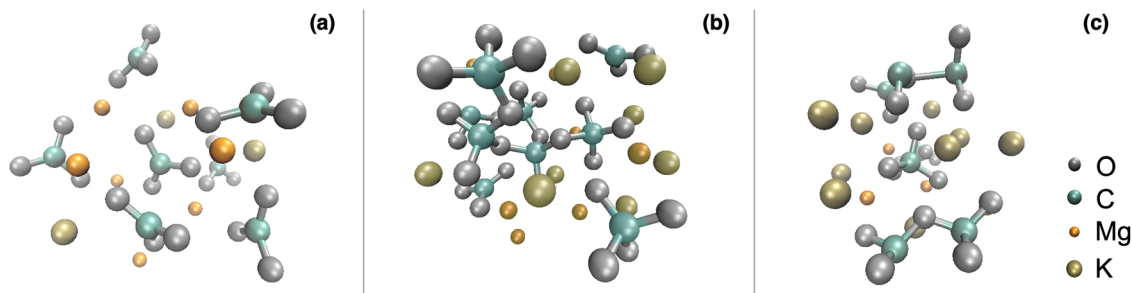


Fig. 2 Atomic structural snapshots from AIMD simulations of $K_2Mg(CO_3)_2$ at different pressures. **a** 4.5 GPa, only CO_3 groups. **b** 106 GPa, co-existing CO_3 and CO_4 units. **c** 145 GPa, all CO_3 groups have been converted to tetracarbonate. Note that $(C_2O_7)^{6-}$ dimers are present already at 106 GPa (**b**) (corresponding to 79 GPa in the experimental spectrum, Fig. 1a). The entire supercell configurations at different pressures are shown in Supplementary Fig. 2.

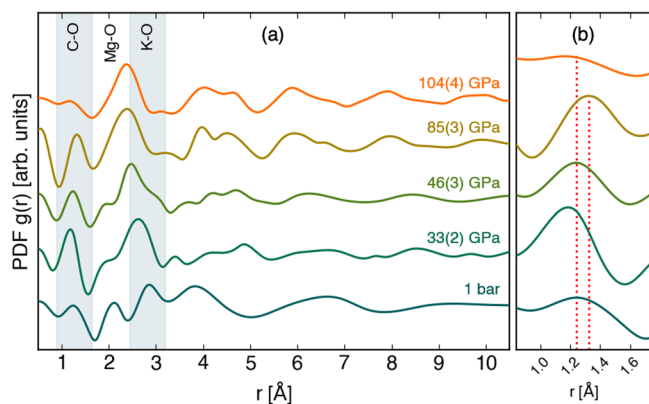


Fig. 3 Pair distribution functions of $K_2Mg(CO_3)_2$ glass at different pressures. The PDFs were obtained by Fourier transforms of the structure factors (Supplementary Fig. 6a). **a** The gray shaded areas highlight the original position of C-O and K-O peaks (Mg-O in between) and emphasize their shift upon compression. **b** Close-up on the C-O peak (representing the bond length distribution).

Geophysical studies suggest that parts of the deep primitive mantle have probably survived through Earth's history and constitute today distinct chemical and geophysical reservoirs at the base of the mantle³² which, most important, might be connected to well known surface processes. Today, seismic tomography reveal the presence of two massive anomalous zones above the core, commonly known as large low velocity provinces (LLVPs), where seismic waves travel slowly. These provinces occupy an area of $\sim 30\%$ of the CMB and are considered to be chemically distinct from the surrounding mantle, formed by a combination of primordial³² or subducted material³³. As discussed in the previous paragraph, the subduction of oceanic crust into the lower mantle may also contribute to create local and highly oxidized pools where the conditions for tetracarbonate groups formation are preserved. Most recent estimations indicate that only $\sim 30\%$ of the subducted carbon is recycled in the crust and atmosphere¹, and even if the associated uncertainties are very large, it is to be expected that at least some of the remaining carbon (in the form of carbonates or other C-carriers) is transported with the oceanic crust further down, ultimately reaching the CMB and thermochemical regions^{32,33}. LLVPs exhibit geographical correlation with hotspot volcanism at the surface, which commonly overlie the edges of the LLVPs, in locations known as ultralow-velocity zones (ULVZ)^{32–36} (Fig. 4). Recent tomographic work suggests the presence of broad conduits of reduced wave velocities beneath some prominent hotspots,

Table 1 Statistical information on the fitting of the PDF peaks as a function of pressure.

P (GPa)	C-O (Å)	Mg-O (Å)	K-O (Å)	C-O (FWHM)
0	1.243 (2)	2.097 (2)	2.848 (6)	0.2915
33 (2)	1.185 (2)	1.939 (7)	2.621 (1)	0.3372
46 (3)	1.236 (1)	1.937 (3)	2.471 (2)	0.3144
85 (4)	1.323 (1)	1.979 (45)	2.406 (23)	0.3709
104 (4)	1.191 (3)	1.982 (8)	2.381 (3)	0.4381

extending from ULVZ at the CMB to roughly ~ 1000 km depth³⁷. The total carbon emissions (e.g. magmatic eruptions and degassing) at these hotspots, e.g. Hawaii, Iceland, and Samoa, are considered to have parental magmatic CO_2 content of the source ranging between 3000 and 10,000 ppm, whereas mid-ocean-ridge (MORBs), which principally sample the convecting upper mantle, around 600 ppm³⁸. Despite the high possible uncertainties in these estimates, hotspot mantle CO_2 concentrations are regarded as distinctly higher than mantle concentrations in all MORB segments located >1000 km from hotspots³⁹. We suggest that localized viscous carbon-rich silicate melts, of primordial and subduction origin, can be stripped away by deep upwelling material to become incorporated in rising plumes^{33,40}, from as deep as the CMB, becoming the possible parental source of intraplate oceanic volcanism and related ocean island basalts (OIBs) (Supplementary Note 2). Upon decompression and depolymerization these C-rich silicate melts become increasingly less viscous and more buoyant also helped by the depolymerization of SiO_x and CO_4 groups^{6–8,17}. Once exhumed to depths <1200 km mechanical factors, such as low melt density, high buoyancy and mantle convection, contribute to the ascent of these carbon-rich melts into the upper mantle and ultimately their degassing into the atmosphere (Fig. 4). Moreover, it is well known that the shallow mantle is more oxidized^{20,21} than the deep mantle, thus during exhumation, reduced carbon-rich silicate melts presumably increase their chance to form oxy-carbon complexes.

It should be also emphasized that increased polymerization at great depths has a strong effect on density and melt rheology. Density estimates indicate that adding up to 5 wt% of CO_2 in a $MgSiO_3$ melt at CMB conditions does not change the melt density sufficiently to make it buoyant with respect to the surrounding mantle¹². Hence, silicate melts could efficiently sequester considerable amounts of carbon and simultaneously preserve the local mechanical stability since they have been found to be denser than the surrounding environment^{7,12}. Thus, it is conceivable that the carbon present in the lowermost part of the lower mantle

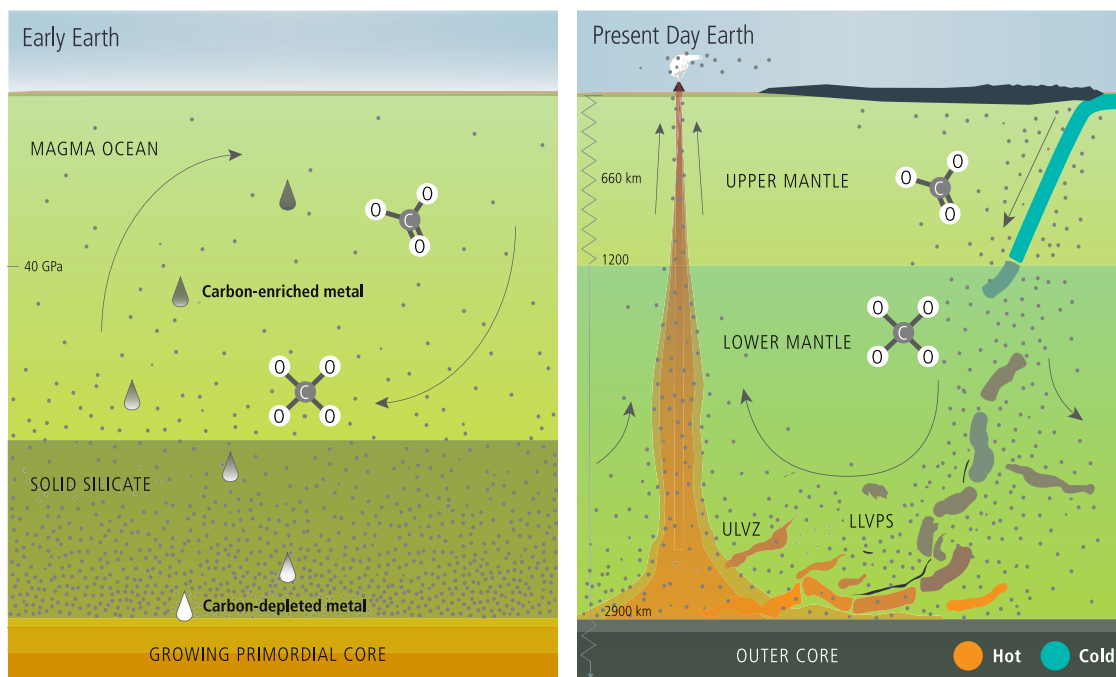


Fig. 4 Distribution and cycling of carbon in the deep mantle during core formation (Early Earth) and in today's Earth (Present Day Earth). Carbon becomes less siderophile with depth and as a consequence is stranded in the lowermost lower mantle as tetracoordinated carbon in silicate melts. With the solidification and convective motions, primordial carbon was accumulated in defined regions at the CMB^{32,33} known as LLVPs and ULVZs. The latter are believed to be the original source of hotspot volcanisms^{33,37}, thus primordial carbon trapped at the CMB could be the primary source of carbon emissions in these locations (Hawaii, Samoa, Pitcairn and many others). Image credit: Josh Wood.

would have reached mechanical stability as a constituent of dense silicate melts and remained confined there.

Conclusions

The correlation of our findings to the most recent data on the deep carbon cycle and geophysical models of Earth's interior leads to suggest the existence of reservoirs of carbon-rich silicate melts at the bottom of the Earth's mantle (LLVPs), which are the largest supply for the carbon-cycle connected to well-known surface processes, i.e. the carbon-rich emissions registered in intraplate volcanism at Hawaii, Samoa, and many others. In these melts, sp^3 hybridized carbon is capable to form tetracarbonate groups, contributing to the development of a 3D network structure. A substantial amount of carbon can be incorporated in silicate melts at the CMB without compromising the gravitational stability, thus it is conceivable to think that tetracarbons actively contribute in the polymerization of silicate melts at those conditions, acknowledging nevertheless that a large part of carbon complexes in those regions could be in a reduced form. Further studies on (i) pure carbonate melts and (ii) carbonated-silicate melts should be performed to corroborate (or confute) the predictions made by simulations.

Methods

Sample selection and preparation. Pure carbonate glass (Supplementary Fig. 8) with composition $K_2Mg(CO_3)_2$ was prepared at the Bayerisches Geoinstitut (BGI) by melting a homogenous and stoichiometric (50:50) mixture of K_2CO_3 and $MgCO_3$ powder in an externally heated rapid-quench cold-seal pressure vessel, at 1 kbar and 700 °C for 12 h. The experiment was terminated by rapid in-situ quenching. High purity (>99.9%) K_2CO_3 was purchased from Alfa Aesar GmbH, dried prior to preparation of the mixture at 110 °C and stored in a drying oven. High purity $MgCO_3$ was kindly provided by the Natural History Museum of London (UK), and dried at 200 °C to ensure dehydration of the Mg carbonate hydrates.

$K_2Mg(CO_3)_2$ -glass was chosen for two reasons, (1) the high Mg content in the glass well reflect the high abundance of Mg in the Earth's interior, hence making it

suitable for experiments looking at simplified natural systems, (2) it is the simplest carbonate-glass stoichiometry quenchable at ambient conditions.

X-ray Raman scattering. The high-pressure X-ray Raman scattering (XRS) spectroscopy experiments (non-resonant inelastic x-ray scattering) were performed at beamline ID20 of the ESRF –The European Synchrotron Radiation Facility (Grenoble, France) using the large solid angle spectrometer⁴¹. We used radiation from four consecutive U26 undulators that was monochromatized by a succession of a high heat-load Si(111) pre- and a Si(311) channel-cut post-monochromator. The monochromatic x-rays were focused onto a spot size of $10 \times 20 \mu m^2$ at the sample position using a Kirkpatrick-Baez (KB) mirror system. The opening angles of the DAC allowed us to use spherically bent Si(660) analyzer crystals: six in the forward and six in the backscattering geometry, respectively. Signals from the forward and backscattering arrays were checked for consistency and averaged for momentum transfers of $2.3 \pm 0.1 \text{ \AA}^{-1}$ in forward scattering and $9.5 \pm 0.1 \text{ \AA}^{-1}$ in backscattering. The incident energy was scanned between values of 10.20 and 10.24 keV in order to obtain energy losses in the vicinity of the oxygen K-edge. All averaged signals were area normalized in the loss-region between 528.0 and 557.0 eV. In all experiments we used BX90 DACs⁴² equipped with 0.5 mm thick miniature diamonds⁴³ and 200 μm and 120 μm diamonds culet size. All diamonds had a 15 μm deep recess drilled in the middle of the culet in order to maximize the x-ray path length through the sample inside the pressure chamber for an increased signal. All data analysis was performed using the XRStools program package^{44,45} as described in Weis et al.⁴⁶. The experimental pressure conditions were estimated offline before and after each XRS measurement based on the Raman signal of the diamonds⁴⁷, with the reported pressures being an average of the two values, and their difference was used as the error estimate.

X-ray diffraction and pair distribution function. The high-pressure x-ray diffraction experiments were performed at beamlines ID15a⁴⁸ and ID15b of the ESRF. Membrane cells with 120 μm culets size provided by the ESRF Sample Environment Service-HP lab were used in both experiments. For each pressure point a new ~50- μm -diameter bead of $K_2Mg(CO_3)_2$ was placed in a wide-aperture membrane cell, fitted with Re gaskets and no pressure medium. For each measurement, both sample and background signals were measured separately and used to calculate the structure factors $S(Q)$, which were obtained by subtraction of the background from the sample patterns (Fig. 5). Background measurements were taken on the DAC containing only the empty gasket after decompression back to ambient conditions, thus maintaining the same gasket thickness as the sample measurement at high pressure. Incident monochromatic x-ray beams with energies of 60 keV ($\lambda = 0.2066 \text{ \AA}$) and 33 keV ($\lambda = 0.4126 \text{ \AA}$) were used for the experiments performed at ID15a and ID15b, respectively. The x-ray beam was focused down to

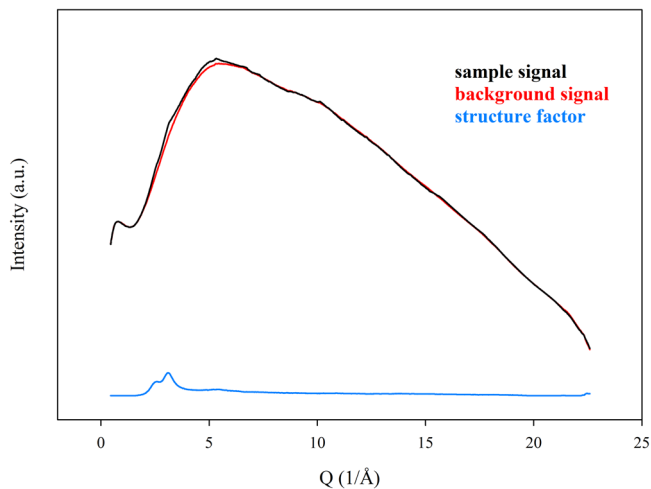


Fig. 5 Graphical representation of the procedure to derive the structure factor from experimental data. The background signal (in red) is subtracted from the sample signal (in black) and the difference is the structure factor $S(Q)$ (in blue). The selected signal was acquired at 46 GPa, while the background was measured at 1 bar using the same gasket, thus same distance between the diamonds, after the sample has been decompressed, removed, and the gasket cleaned in ultrasonic bath.

$3 \times 3 \mu\text{m}^2$ at ID15a using a Kirkpatrick-Baez mirror system (KB) and to $10 \times 10 \mu\text{m}^2$ at ID15b using Compound Refractive Lenses (CRLs). Diffraction data were collected with a Dectris Pilatus3 X CdTe 2 M detector at ID15a and a MAR555 image plate detector at ID15b. Pilatus3X and MAR555 detectors were placed at 250 mm and 260 mm from the sample. A 20 μm pinhole was mounted at the entrance of the DAC to cut background air scattering. The detector-sample distance and the detector tilt angle were calibrated using LaB_6 and silicon standards for ID15a and ID15b, respectively. Contrary to the MAR555 detector, which was centered with respect to the transmitted direct beam, the Pilatus detector was off-centered, allowing a higher Q -range to be detected. The typical collection time was of ~ 8 min at ID15a and 30 min at ID15b. A comparison example between structure factors measured at ID15a and ID15b at ~ 30 GPa are displayed in Supplementary Fig. 9. As one can notice, the two curves nearly coincide, and most importantly, the onset of the first and second sharp diffraction peaks, FSDP and SSDP respectively, coincide.

Because of the larger high quality Q -range obtained from structure factors measured at ID15a (larger detector placed off of the sample center, higher energy), we decided to calculate the x-ray Pair Distribution Functions (PDFs) only from those data. The structure factors collected at ID15b were used, together with those from ID15a, to perform analyses on the FSDP and SSDP, of the $S(Q)$ (Supplementary Figs. 6 and 10). Data for PDF analysis were collected at each pressure in 128 exposures of 4 s each. Particular care was taken during cell loadings to ensure reproducible positions of the diamond Bragg reflections on the detector between sample and background measurements. For each sample dataset the median image was calculated and we subtracted the corresponding median background image. Azimuthal integration to yield $I(Q)$ diffraction patterns was done using pyFAI⁴⁹. From each $I(Q)$ the PDF, $g(r)$, was calculated using PdfGetX⁵⁰. The range of Q for $g(r)$ calculations was $0.8 \leq Q \leq 12 \text{ \AA}^{-1}$. In order to obtain a reliable PDF from weak, noisy signal, ad-hoc intensity weighting and smoothing of the Q -space input functions were used to remove artifacts such as e.g. ripples, associated with parasitic scattering, particularly generated by the tails of diamond peaks. While peak intensities might not be very precise due to the difficulties of estimating against an unknown background, i.e. consequence of DAC setup, the peak positions are considered to be correct. Thus, we explain the distinguished intensity drop of the C-O peak of the PDF at 104 GPa (Fig. 3), attributed to the PDF generation process.

Ab initio molecular dynamics simulations. First-principles molecular dynamics (FPMD) calculations were performed using the Vienna Ab initio Simulation Package (VASP)⁵¹ based on the density functional theory. Effects of the core electrons were replaced by atomic projected augmented wave (PAW) potentials⁵². Valence electronic configurations of $3s^23p^64s^1$, $3s^23p^64s^2$, $2s^22p^2$, and $2s^22p^4$ were used for K, Mg, C, and O atoms, respectively. The Perdew-Burke-Ernzerhof (PBE) exchange-correlation function⁵³ was used. The wave functions were represented by a plane-wave basis set with an energy cutoff of 495 eV. To generate the glass structure of $\text{K}_2\text{Mg}(\text{CO}_3)_2$ at ambient pressure and ambient temperature, a supercell containing 176 atoms ($16 \text{ K}_2\text{Mg}(\text{CO}_3)_2$ formula units) was initially melted at

2000 K for 30 ps with a time step of 1 fs in the canonical ensemble (NVT). The Nose-Hoover thermostat was used to control the temperature. A single point was used for Brillouin zone sampling. Then the molten structure was gradually cooled to 300 K in 10 ps and followed by a NVT MD run at 300 K for at least another 30 ps. Higher pressure glass structures were obtained by isotropically reducing the cell size step by step. Due to the limited cell size and time duration of the MD calculation, over-heating is usually needed for the occurrence of the structural transformation in such closed system. Thus, the high pressure structure (above 28 GPa) were annealed at 4000 K for 30 ps and then quenched to 300 K. To eliminate anisotropy in the stress tensors from the NVT calculation, the isothermal-isobaric ensemble (NPT calculation) was employed on the quenched glass structures for an additional 20 ps. In agreement with experimental observations, structural analysis of the atomic configurations show 4-fold C-O coordination starting to appear at pressures higher than 58 GPa. The amount of 3- and 4-coordinated C-O are almost equal at 106 GPa, which correspond to an experimental pressure of ~ 80 GPa (Fig. 1a and Supplementary Fig. 1). At 145 GPa, the highest pressure considered here, 4-coordinated C-O becomes dominant. Snapshots extracted from the NPT MD trajectories were used in the computation of the XRS spectra (Fig. 1a).

BSE spectral calculations. All spectrum simulations were performed based on structural snapshots from the ab initio molecular dynamics simulation trajectories described in the previous sub-section using the Bethe-Salpeter Equation (BSE) method as implemented in the OCEAN code (Obtaining Core level Excitations using Ab initio methods and the NIST BSE solver)^{54,55}. For each of the spectra presented in Fig. 1, we used 10 snapshots at regularly spaced time intervals of a few ps and evaluated the O K-edge for each of the 96 O atoms for a total of 960 individual O K-edge spectra at each pressure point.

Ground state electronic densities and wave functions were calculated at the density functional theory (DFT) level using Quantum ESPRESSO⁵⁶. All DFT calculations were performed within the local density approximation (LDA) to the exchange-correlation functional, and using norm conserving pseudopotentials taken from the ABINIT repository. A planewave energy cutoff of 70 Ry and Gamma-point sampling for the ground state electron density proved to be sufficient. The wave functions for the screening and BSE calculation were generated from a non-self-consistent-field calculation using a $2 \times 2 \times 2$ k-point mesh. We used projector augmented wave (PAW)⁵² reconstructed all electron wave functions for the calculation of core to valence transition matrix elements. The dielectric screening was evaluated in within a sphere centered around every scattering atom using the random phase approximation and using the Levine-Louie model dielectric function outside this sphere. Convergence of the final spectra with respect to the change over radius^{52,57} was confirmed. Final electron-hole scattering states are obtained by solving the BSE.

Data availability

Experimental and simulation-derived datasets are publicly available in EarthChem repository (<https://www.earthchem.org/>). The unique identifiers (DOIs) are assigned to datasets collected at different beamlines as follow: i) ID15a 10.26022/IEDA/112756, ii) ID15b 10.26022/IEDA/112757 and 10.26022/IEDA/112758, iii) ID20 10.26022/IEDA/112759 and 10.26022/IEDA/112760, iv) simulations (RDF) 10.26022/IEDA/112761.

Code availability

Ab-initio molecular dynamics simulations and spectra calculations were performed using VASP (v. 5.4.4, <https://www.vasp.at>) and OCEAN (<http://monalisa.phys.washington.edu/OCEAN/>) program packages respectively, which are available and free to use under standard license. All analysis scripts are available from the corresponding author upon request.

Received: 1 August 2022; Accepted: 21 February 2023;
Published online: 17 March 2023

References

- Plank, T. & Manning, C. E. Subducting carbon. *Nature* **574**, 343–352 (2019).
- Poli, S. Carbon mobilized at shallow depths in subduction zones by carbonatitic liquids. *Nat. Geosci.* **8**, 633–636 (2015).
- Kono, Y. et al. Ultralow viscosity of carbonate melts at high pressures. *Nat. Commun.* **5**, 5091 (2014).
- Gaillard, F., Malki, M., Iacono-Marziano, G., Pichavant, M. & Scaillet, B. Carbonatite melts and electrical conductivity in the asthenosphere. *Science* **322**, 1363–1365 (2008).
- Jones, A. P., Genge, M. & Carmody, L. Carbonate melts and carbonatites. *Rev. Mineral. Geochem.* **75**, 289–322 (2013).

6. Sanloup, C. et al. Structural change in molten basalt at deep mantle conditions. *Nature* **503**, 104–107 (2013).
7. Petitgirard, S. et al. Fate of MgSiO₃ melts at core–mantle boundary conditions. *Proc. Natl Acad. Sci. USA* **112**, 14186–14190 (2015).
8. Prescher, C. et al. Beyond sixfold coordinated Si in SiO₂ glass at ultrahigh pressures. *Proc. Natl Acad. Sci. USA* **114**, 10041–10046 (2017).
9. Wood, B. J., Walter, M. J. & Wade, J. Accretion of the Earth and segregation of its core. *Nature* **441**, 825–833 (2006).
10. Blanchard, I. et al. The metal–silicate partitioning of carbon during Earth’s accretion and its distribution in the early solar system. *Earth Planet. Sci. Lett.* **580**, 117374 (2022).
11. Fischer, R. et al. The carbon content of Earth and its core. *Proc. Natl Acad. Sci. USA* **117**, 8743–8749 (2020).
12. Ghosh, D. B. et al. Carbon-bearing silicate melt at deep mantle conditions. *Sci. Rep.* **7**, 848 (2017).
13. Solomatova, N. V., Caracas, R. & Manning, C. E. Carbon sequestration during core formation implied by complex carbon polymerization. *Nat. Commun.* **10**, 789 (2019).
14. Karki, B. B., Ghosh, D. B. & Banjara, D. Mixed incorporation of carbon and hydrogen in silicate melts under varying pressure and redox conditions. *Earth Planet. Sci. Lett.* **549**, 116520 (2020).
15. Stöhr, J. “*Symmetry and Molecular Orbitals*” in *NEXAFS Spectroscopy* (Springer-Verlag Berlin Heidelberg, 1992). p. 48–78.
16. Cerantola, V. et al. Stability of iron-bearing carbonates in the deep Earth’s interior. *Nat. Commun.* **8**, 15960 (2017).
17. Ghosh, D. B., Karki, B. B. & Stixrude, L. First-principles molecular dynamics simulations of MgSiO₃ glass: Structure, density, and elasticity at high pressure. *Am. Mineral.* **99**, 1304–1314 (2014).
18. Wood, B. J., Li, J. & Shahar, A. Carbon in the core: Its influence on the properties of core and mantle. *Rev. Mineral. Geochem.* **75**, 231–250 (2013).
19. Li, J., Chen, B., Mookherjee, M. & Morar, G. *Deep Carbon*. 1st edn. (Cambridge University Press, Cambridge, 2020) p. 40–65.
20. McCammon, C. The paradox of mantle redox. *Science* **308**, 807–808 (2005).
21. Frost, D. J. & McCammon, C. A. The redox state of Earth’s mantle. *Ann. Rev. Earth Planet. Sci.* **36**, 389–420 (2008).
22. Frost, D. J. et al. Experimental evidence for the existence of iron-rich metal in the Earth’s lower mantle. *Nature* **428**, 409–412 (2004).
23. Armstrong, K., Frost, D. J., McCammon, C. A., Rubie, D. C. & Boffa-Ballaran, T. Deep magma ocean formation set oxidation state of Earth’s mantle. *Science* **365**, 903–906 (2019).
24. Deng, J., Du, Z., Karki, B. B., Ghosh, D. B. & Lee, K. K. M. A magma ocean origin to divergent redox evolutions of rocky planetary bodies and early atmospheres. *Nat. Commun.* **11**, 2007 (2020).
25. Andraut, D. et al. Large oxygen excess in the primitive mantle could be the source of the Great Oxygenation Event. *Geochem. Perspect. Lett.* <https://doi.org/10.7185/geochemlet.1801> (2018).
26. Bekker, A. & Holland, H. D. Oxygen overshoot and recovery during the early Paleoproterozoic. *Earth Planet. Sci. Lett.* **317**, 295–304 (2012).
27. Fischer-Gödde, M. et al. Ruthenium isotope vestige of Earth’s pre-late-veener mantle preserved in Archaean rocks. *Nature* **579**, 240–244 (2020).
28. Albarède, F. Volatile accretion history of the terrestrial planets and dynamic implications. *Nature* **461**, 1227–1233 (2009).
29. Stagno, V., Tange, Y., Miyajima, N., McCammon, C. A. & Frost, D. J. The stability of magnesite in the transition zone and the lower mantle as function of oxygen fugacity. *Geophys. Res. Lett.* **38**, L19309 (2011).
30. Dasgupta, R. & Hirschmann, M. M. The deep carbon cycle and melting in Earth’s interior. *Earth Planet. Sci. Lett.* **298**, 1–13 (2010).
31. Dorfman, S. M. et al. Carbonate stability in the reduced lower mantle. *Earth Planet. Sci. Lett.* **489**, 84–91 (2018).
32. Panchai, S., Li, M., Thorne, S. M., Dettmer, J. & Tkalčić, H. Internal structure of ultralow-velocity zones consistent with origin from a basal magma ocean. *Nat. Geosci.* **15**, 79–84 (2022).
33. Garnero, E. J., McNamara, A. K. & Shim, S.-H. Continent-sized anomalous zones with low seismic velocity at the base of Earth’s mantle. *Nat. Geosci.* **9**, 481–489 (2016).
34. Li, M. & McNamara, A. K. Evolving morphology of crustal accumulations in Earth’s lowermost mantle. *Earth Planet. Sci. Lett.* **577**, 117265 (2022).
35. Helmberger, D., Wen, L. & Ding, X. Seismic evidence that the source of the Iceland hotspot lies at the core–mantle boundary. *Nature* **396**, 251–255 (1998).
36. Cottaar, S. & Romanowicz, B. An unusually large ULVZ at the base of the mantle near Hawaii. *Earth Planet. Sci. Lett.* **355–356**, 213–222 (2012).
37. French, S. W. & Romanowicz, B. Broad plumes rooted at the base of the Earth’s mantle beneath major hotspots. *Nature* **525**, 95–99 (2015).
38. Hauri, E. H. et al. *Deep Carbon*. 1st edn (Cambridge University Press, Cambridge, 2020) p. 40–65.
39. Le Voyer, M. et al. Carbon fluxes and primary magma CO₂ contents along the global mid-ocean ridge system. *Geochem. Geophys. Geosyst.* **20**, 1387–1424 (2019).
40. Ballmer, M. D. et al. Persistence of strong silica-enriched domains in the Earth’s lower mantle. *Nat. Geosci.* **10**, 236–240 (2017).
41. Huotari, S. et al. A large-solid-angle X-ray Raman scattering spectrometer at ID20 of the European Synchrotron Radiation Facility. *J. Synchrotron Radiat.* **24**, 521–530 (2017).
42. Kantor, I. et al. BX90: a new diamond anvil cell design for X-ray diffraction and optical measurements. *Rev. Sci. Instrum.* **83**, 125102 (2012).
43. Petitgirard, S. et al. Miniature diamond anvils for X-ray Raman scattering spectroscopy experiments at high pressure. *J. Synchrotron Radiat.* **24**, 276–282 (2017).
44. Sahle, C. J. et al. Planning, performing and analyzing X-ray Raman scattering experiments. *J. Synchrotron Radiat.* **22**, 400–409 (2015).
45. Sahle, C. J. et al. Improving the spatial and statistical accuracy in X-ray Raman scattering based direct tomography. *J. Synchrotron Radiat.* **24**, 476–481 (2017).
46. Weis, C. et al. Pressure driven spin transition in siderite and magnesiosiderite single crystals. *Sci. Rep.* **7**, 16526 (2017).
47. Akahama, Y. & Kawamura, H. Pressure calibration of diamond anvil Raman gauge to 310 GPa. *J. Appl. Phys.* **100**, 043516 (2006).
48. Vaughan, G. et al. ID15A at the ESRF, a beamline for high speed operando X-ray diffraction, diffraction tomography, and total scattering. *J. Synchrotron Radiat.* **27**, 515–528 (2020).
49. Ashiotis, G. et al. The fast azimuthal integration Python library: pyFAI. *J. Appl. Crystallogr.* **48**, 510–519 (2015).
50. Juhás, P. et al. PDFgetX3: a rapid and highly automatable program for processing powder diffraction data into total scattering pair distribution functions. *J. Appl. Crystallogr.* **46**, 560–566 (2013).
51. Kresse, G. & Furthmüller, J. Efficient iterative schemes for ab initio total-energy calculations using a plane-wave basis set. *Phys. Rev. B* **54**, 16 (1996).
52. Kresse, G. & Joubert, D. From ultrasoft pseudopotentials to the projector augmented-wave method. *Phys. Rev. B* **59**, 1758 (1999).
53. Perdew, J. P., Burke, K. & Ernzerhof, M. Generalized gradient approximation made simple. *Phys. Rev. Lett.* **77**, 18 (1996).
54. Vinson, J., Rehr, J. J., Kas, J. J. & Shirley, E. L. Bethe-Salpeter equation calculations of core excitation spectra. *Physical Review B* **83**, 115106 (2011).
55. Gilmore, K. et al. Efficient implementation of core-excitation Bethe–Salpeter equation calculations. *Comput. Phys. Commun.* **197**, 109–117 (2015).
56. Giannozzi, P. et al. QUANTUM ESPRESSO: a modular and open-source software project for quantum simulations of materials. *J. Phys. Condens. Matter* **21**, 395502 (2009).
57. Levine, Z. H. & Louie, S. G. New model dielectric function and exchange-correlation potential for semiconductors and insulators. *Phys. Rev. B* **25**, 6310 (1982).

Acknowledgements

We acknowledge the ESRF for providing synchrotron radiation and technical support at ID20, ID15a, and ID15b beamlines. We acknowledge the helpful support of the Sample Environment Service-HP lab. C. Henriquet is gratefully acknowledged for providing technical support at beamline ID20. We are thankful to C. Cavallari and M. Apollo for support during the first XRS experiment. We acknowledge R. Ruffer and A. Chumakov for providing the diamonds used in the experiments. MiW thanks the support by the National Natural Science Foundation of China (51701180, U1802254, 51871201). Part of the work was performed with the support of Project MIUR - Dipartimenti di Eccellenza TECLA, Department of Earth and Environmental Sciences, University of Milano-Bicocca.

Author contributions

V.C. conceptualized the project. V.C., C.J.S., and S.P. interpreted the results and wrote the manuscript with contributions of all authors. R.A., S.P., and Ma.W. synthesized the sample. V.C., C.J.S., S.P., and C.W. performed the XRS experiments. V.C., C.J.S., S.P., S.C., G.V., M.D.M., M.H., and I.E.C. performed the XRD experiment. C.W. and C.J.S. analyzed XRS data. S.C., G.V., M.D.M., S.P., and V.C. analyzed XRD data. Mi.W. and J.S.T. performed AIMD simulations. C.J.S. performed BSE calculations. A.P.J. contributed to selection of carbonate glass.

Funding

Open Access funding enabled and organized by Projekt DEAL.

Competing interests

The authors declare no competing interests.

Additional information

Supplementary information The online version contains supplementary material available at <https://doi.org/10.1038/s43247-023-00722-8>.

Correspondence and requests for materials should be addressed to Valerio Cerantola.

Peer review information *Communications Earth & Environment* thanks Bijaya Karki and the other, anonymous, reviewer(s) for their contribution to the peer review of this work. Primary Handling Editor: Joe Aslin. Peer reviewer reports are available.

Reprints and permission information is available at <http://www.nature.com/reprints>

Publisher's note Springer Nature remains neutral with regard to jurisdictional claims in published maps and institutional affiliations.



Open Access This article is licensed under a Creative Commons Attribution 4.0 International License, which permits use, sharing, adaptation, distribution and reproduction in any medium or format, as long as you give appropriate credit to the original author(s) and the source, provide a link to the Creative Commons license, and indicate if changes were made. The images or other third party material in this article are included in the article's Creative Commons license, unless indicated otherwise in a credit line to the material. If material is not included in the article's Creative Commons license and your intended use is not permitted by statutory regulation or exceeds the permitted use, you will need to obtain permission directly from the copyright holder. To view a copy of this license, visit <http://creativecommons.org/licenses/by/4.0/>.

© The Author(s) 2023